This is the accepted version of the following article: Ji X*, Luo RW, Zhuang YC, Gao X, Lim WH, Qu Z. Seismic behavior of a stone curtain wall system with undercut bolt anchorage under various loading protocols. *Earthquake Engineering & Structural Dynamics*. This article may be used for non-commercial purposes.

Seismic behavior of a stone curtain wall system with undercut bolt anchorage under various loading protocols

Xiaodong Ji[1*], Rongwei Luo[1], Yuncheng Zhuang[1], Xiang Gao[1], Wanhui Lim[1], Zhe Qu[2]

[1]Key Laboratory of Civil Engineering Safety and Durability of China Education Ministry, Department of Civil Engineering, Tsinghua University, Beijing 100084, China

[2]Key Laboratory of Earthquake Engineering and Engineering Vibration, Institute of Engineering Mechanics, CEA, Sanhe, Hebei 065201, China

Abstract

This paper presents full-scale experimental tests on the seismic behavior of a stone curtain wall system with undercut bolt anchorage (SCWS-UBA). Experimental set-ups were developed to test full-scale stone curtain wall systems subjected to three loading protocols: quasi-static in-plane loading, dynamic in-plane loading, and dynamic coupled in-plane and out-of-plane loading. In all three tests, the SCWS-UBA failed due to connector disengagement, followed by fracture of silicone sealant and transom-to-mullion connection welds and, finally, the falling out of stone panels. The SCWS-UBA specimens exhibited a large displacement capacity with an ultimate falling out drift exceeding 3.0% in all tests. The drift ratio at connector disengagement was almost identical for both quasi-static and dynamic in-plane loading scenarios, indicating that in-plane accelerations had a minimal impact on stone curtain wall failure. In addition, disengagement of the connector was dependent on the horizontal edge distance and vertical overlap depth between the connector and the L-shaped steel angle. Simplified formulas for calculating the horizontal and vertical displacement of the connector were then developed. Based on these, seismic design recommendations were proposed for the overlap depth and edge distance between the connector and L-shaped steel angle, thereby preventing the falling out of stone panels.

KEYWORDS

stone curtain wall, undercut bolt anchorage, seismic behavior, drift capacity, design recommendation

1 INTRODUCTION

The stone curtain wall system (SCWS), known for its elegant appearance, excellent durability and environmentally-friendly performance has been widely adopted in buildings. In recent years, the dry-hanging method has grown in popularity for SCWS construction. This method involves the use of a high-strength and corrosion-resistant metal pendant to directly hang stone panels onto the outer surface of the building structure, leaving a gap between the stone and the structure. One of the most commonly used types of SCWS is the stone curtain wall with undercut bolt anchorage (SCWS-UBA), in which the stone panels are connected to the supporting frame through undercut bolts and connectors. This connection type allows for flexible three-dimensional adjustment and is convenient for installation and replacement.

Past earthquakes such as the 1985 Mexico earthquake [1][1], the 1987 California earthquake [2][1], the 1994 Northridge earthquake[2] [3] and the 2011 Christchurch earthquake [4] [3]have resulted in severe seismic damage to the SCWS [5]-[7][6]. The observed damage includes the breakage and falling out of stone panels and the failure of connection components. Such damage can lead to significant financial losses, and the falling out of stone panels may even result in human casualties. Notably, the stone panels mainly fall out due to the failure of nuts, dowels, brackets or other connection components [8][7].

To prevent damage to the SCWS-UBA, some standards impose the requirements on the flexural strength of stone panels and the capacity of the undercut bolt. According to the Chinese standard JGJ 133-2001 [9][8], the flexural strength of stone panels should be no less than 8.0 MPa. In the United States, ASTM C615-11 [10] [9]specifies that the flexural strength of stone panels should be greater than 8.27 MPa. Additionally, Chinese standard DB11-T 512-2007 [11] [10]specifies the requirements for the anchorage tensile and shear strength for the undercut bolt, while ACI 318-19[11] [12] and CSA A23.3 [13] [12]standards require anchor bolt designs for tensile and shear loads. However, the seismic design detailing of connectors is not adequately provided in these standards.

Experimental tests have been conducted in order to investigate the seismic performance of the SCWS-UBA and its connection behavior. For instance, Gao et al. [14] [13]and Zhang et al. [15] [14]identified important factors that influence the connection strength of undercut bolts through a series of pull-out tests. Huang et al. [16]

[*] Corresponding author: Xiaodong Ji, Professor of Tsinghua University, email: jixd@mail.tsinghua.edu.cn

[15]performed a full-scale shaking table test to investigate the seismic performance of granite claddings with undercut bolt anchorage, the results of which revealed that the aluminum connectors are the most seismically vulnerable components of the cladding system. Fan et al. [17] [16]conducted full-scale shaking table tests of a novel granite façade system with undercut bolt anchorage. When the peak drift ratio of 0.4% was attained under seismic shaking, sliding of the panels and deformation of the bolts were observed. Lu et al. [18] [17]conducted a shaking table test of an artificial stone cladding with undercut bolt anchorage. At 2.0% drift, the fastening bolts of the connectors loosened, leading to detachment of the connectors. In addition, during full-scale shaking table tests of SCWS-UBA specimens [19]-[22], [18]which were subjected to a maximum inter-story drift of 1% to 2%, the connections slid and the stone panels experienced sliding and collisions, despite the stone panels did not fall out. To summarize, no overall failure of the SCWS has been observed in existing shaking table tests due to the limited loading drift. This makes it difficult to determine the ultimate drift capacity and failure modes of the SCWS. In addition, the tested specimens were mostly single large-sized stone panels or one to two columns of large stone panel units, which may not reasonably simulate the actual interaction among surrounding panels.

In this study, in-plane cyclic racking tests loaded using a dynamic actuator and coupled in-plane and out-of-plane cyclic racking tests loaded using a shaking table were conducted on a full-scale SCWS-UBA. The novel contributions of this research are as follows: (1) developing test set-ups and the corresponding methods for a full-scale SCWS-UBA, including in-plane loading and coupled in-plane and out-of-plane loading; (2) examining the seismic behavior and failure modes of a full-scale SCWS-UBA with multiple rows and columns; and (3) proposing design recommendations for the SCWS-UBA connection.

This paper is structured as follows. The second section presents the experimental program for a full-scale SCWS-UBA, highlighting various loading set-ups and loading protocols. The third section describes the results of the experimental tests. The fourth section presents design recommendations for the connector details to ensure the seismic safety of the SCWS-UBA.

2 EXPERIMENTAL PROGRAMS

2.1 Experimental specimens

The specimens represented a typical SCWS, consisting of stone panels, undercut bolts, aluminum alloy connectors, and supporting frames composed of transoms and mullions. The SCWS was designed and installed by a professional curtain wall company in accordance with typical engineering practices in China. For the in-plane loading test by the dynamic actuator, the specimen (denoted SCW1) was installed outside the steel loading frame which consisted of six rows and six columns of stone panel units. SCW1 had a total height of 3.50 m and a width of 5.00 m (FIGURE 1a). In the shaking table loading test, the specimen (denoted SCW2) was installed inside the steel loading frame to prevent the stone panels from falling out of the shaking table, thereby ensuring that the test was safe. SCW2 consisted of four rows and four columns of stone panel units, with a total height of 2.40 m and a width of 3.60 m (FIGURE 1b). Each stone panel was connected to its surrounding panels by silicone sealant.

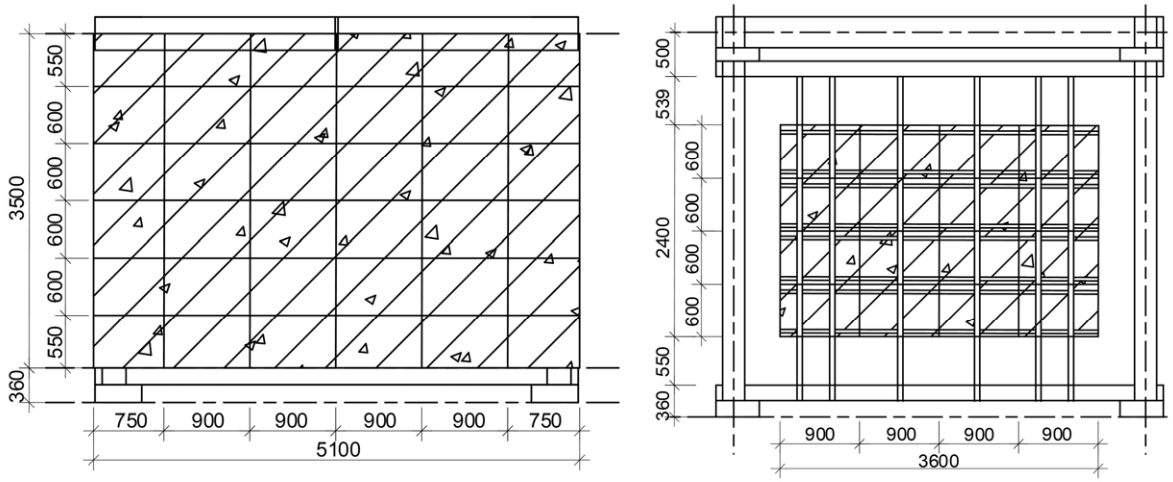

(a) Elevation view of SCW1 (b) Elevation view of SCW2

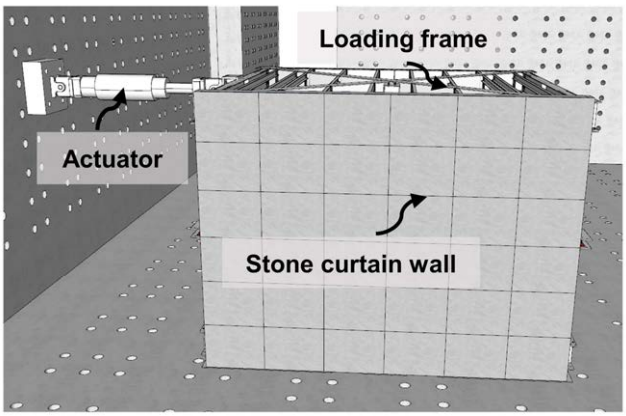

(c) Schematic view of SCW1

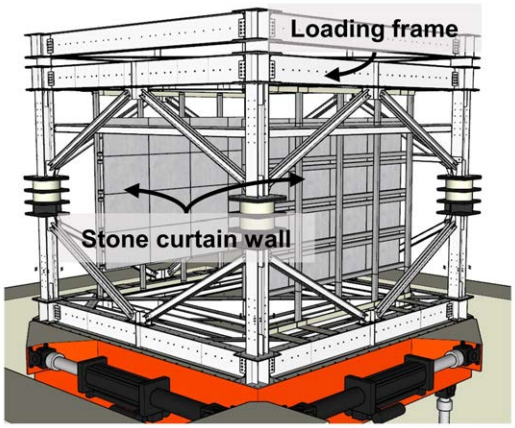

(d) Schematic view of SCW2

FIGURE 1 Elevation and schematic view of specimens

The thickness of stone panel units was uniformly 25 mm. In specimen SCW1, there were four different sizes of individual stone panels: 750 mm × 550 mm, 750 mm × 600 mm, 900 mm × 550 mm, and 900 mm × 600 mm. In specimen SCW2, the dimensions of the stone panels were uniformly 900 mm × 600 mm. FIGURE 2 depicts the details of the stone curtain wall connections. Each stone panel was connected to the transoms with four undercut bolts and four aluminum alloy connectors. The undercut bolt M6 (diameter = 6 mm) was embedded 11 mm into the stone panel. The undercut bolt was connected to the aluminum alloy connector through a nut, a washer, and a rubber gasket. The stone panel was hung on 77 mm long L-shaped steel angles (height × width × thickness = 50 mm × 50 mm × 5 mm) through connectors. The connector had the length, height and thickness of 47 mm, 53 mm and 4 mm, respectively. Gaskets were placed to fill the gap between the connector and the L-shaped angle steel. The L-shaped steel angle was connected to the transom through two M6 bolts, while the transom was connected to the mullion via fillet welds. The transoms were made by steel angle (height × width × thickness = 50 mm × 50 mm × 4 mm), and the mullions were fabricated by rectangular steel tube (height × width × thickness = 80 mm × 40 mm × 4 mm). TABLE 1 presents the material properties of the components and connectors of the specimens.

TABLE 1 Material properties

Member	Material grade	Nominal yield strength / (MPa)	Young's modulus / (MPa)	Poisson's ratio
Mullion	Q235 steel	235	2.1×10^5	0.30
Transom	Q235 steel	235	2.1×10^5	0.30
L-shaped steel angle	Q235 steel	235	2.1×10^5	0.30
Connector	Aluminum 6063-T5	160	0.7×10^5	0.33
Stone panel	Granite MU150	/	0.8×10^5	0.125
M6 bolt	Grade 4.8	320	2.1×10^5	0.30

Note: the nominal compressive strength of the Granite MU150 stone is 150 MPa.

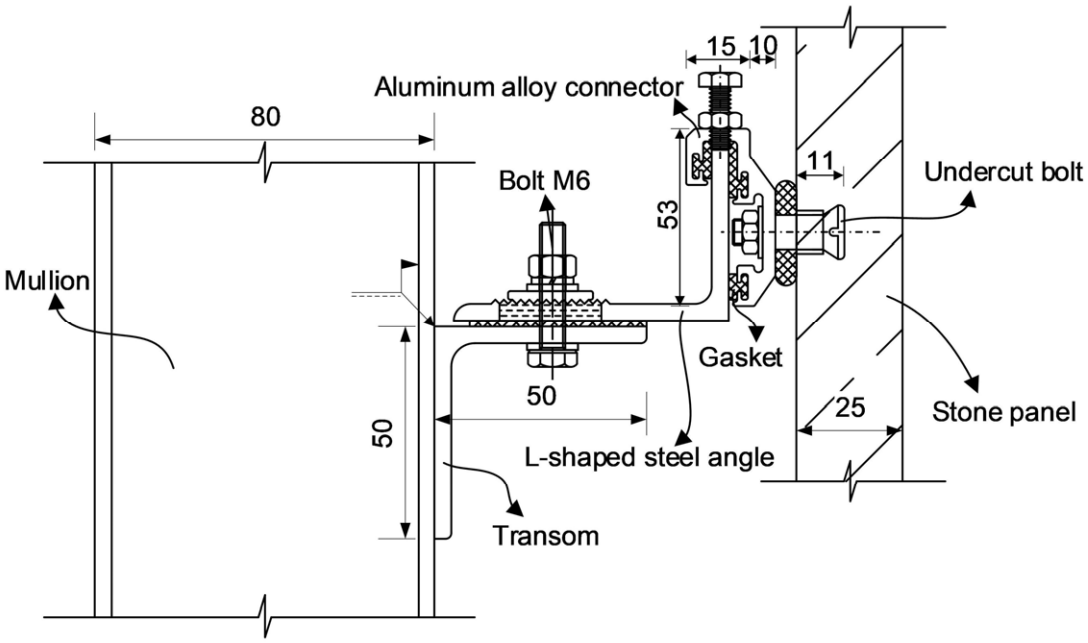

(a) Elevation view (units in mm)

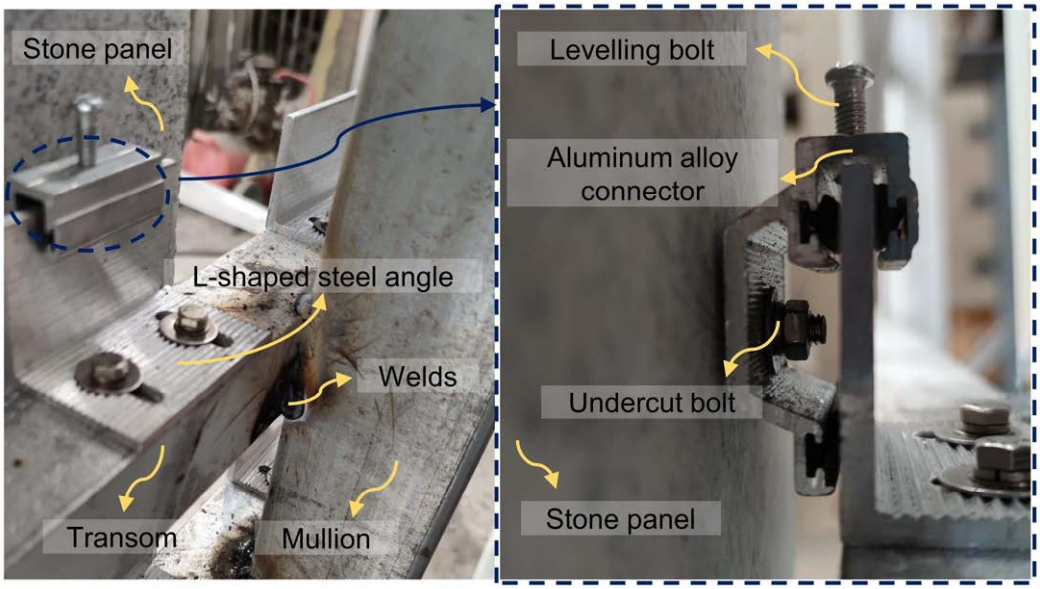

(b) Photographs

FIGURE 2 Stone curtain wall connections

2.2 Test set-up

Two test set-ups for loading curtain wall systems, as reported in Ji et al. [23][22], were used in this study, one for in-plane loading by an actuator and the other for bidirectional loading by a shaking table.

2.2.1 In-plane loading set-up

FIGURE 3a displays the in-plane loading set-up. On both the north and south sides of the loading frame, a six-row by six-column SCWS was installed. The mullions of the SCWS were fastened by a pair of clip angles at their both ends and then connected to the steel channel beams at the top and base levels of the loading frame. The steel channel beams were securely attached to the loading frame through the cantilevered short steel channel and steel angle (see FIGURE 4). The foundation beams of the loading frame were securely fixed to the strong floor, and the top beam of the loading frame was linked to a horizontal dynamic hydraulic actuator which could apply a lateral displacement time history. Columns in the loading frame were separated into upper and lower components connected by a low-friction linear guideway, which ensured large cyclic displacement of the loading frame in the direction of the guideway. During the lateral cyclic loading, the SCWS sustained the lateral drift and acceleration

demands identical to those of the loading frame. String potentiometers were used to measure the lateral displacement— these were installed on the top and bottom beams of the loading frame and at various heights of the stone curtain wall. In addition, accelerometers were placed on the top beams of the loading frame and SCWS to measure the acceleration responses.

2.2.2 Bidirectional loading set-up

FIGURE 3b depicts the bidirectional loading set-up. A four-row by four-column SCWS was installed on the north and south sides of the loading frame, respectively. The SCWS was attached to the beams at the top and base levels of the loading frame, and the foundation beams of the loading frame were fixed onto the 5 m by 5 m shaking table. Instead of linear guideways, rubber bearings were installed in the middle of the frame columns to achieve both in-plane and out-of-plane loading. Steel plates and blocks with a mass of 2×10^4 kg were placed on top of the loading frame to generate horizontal inertial forces. The loading frame was motivated by the motion of the shaking table, and the lateral drift and acceleration of the loading frame were transmitted to the SCWS. String potentiometers were installed on the top and bottom beams of the loading frame and curtain walls to measure in-plane and out-of-plane lateral displacement. Four three-axis accelerometers were placed on the bottom and top beams of the loading frame to record table input and system acceleration responses.

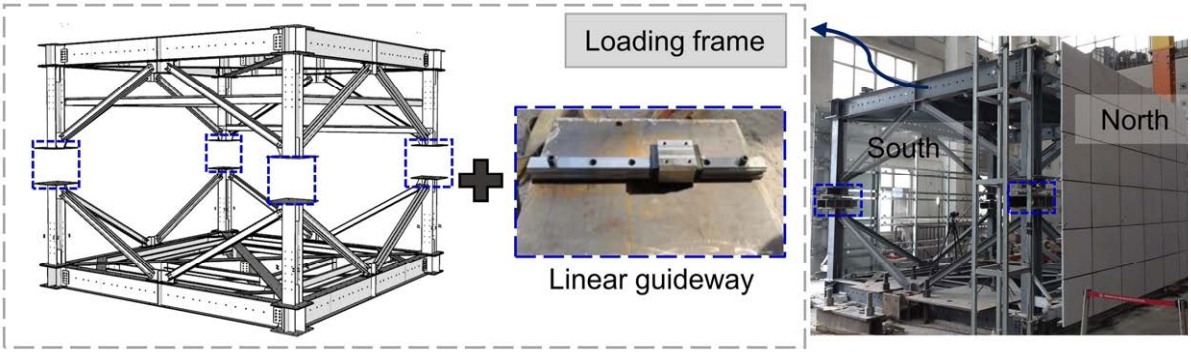

(a) In-plane loading set-up

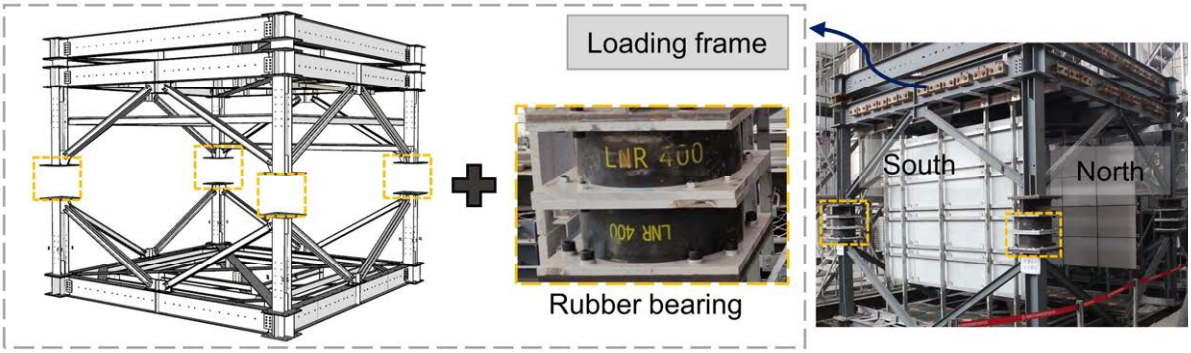

(b) Bidirectional loading set-up

FIGURE 3 Schematic drawing and photographs of loading set-up

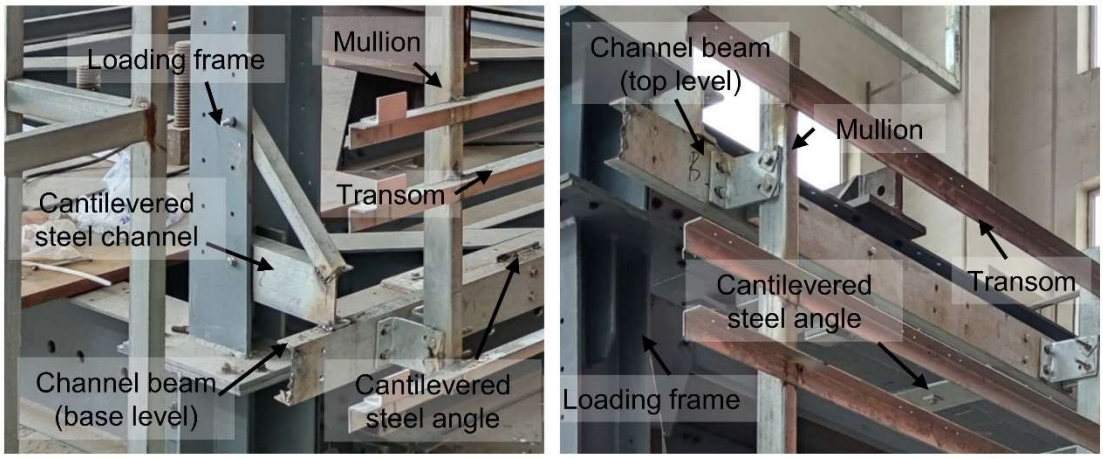

FIGURE 4 Photographs of attachment of SCWS-to-loading frame

2.3 Loading protocols

Three loading protocols were employed in this study to compare the effect of in-plane versus coupled in-plane and out-of-plane loading, and dynamic loading versus static loading, on the performance of the SCWS-UBA. The loading protocols were identical to those used by Ji et al. [23]: [22]namely, (i) FEMA 461 quasi-static loading protocol; (ii) AAMA 501.6-01 dynamic loading protocol; and (iii) bidirectional AAMA 501.6-01 dynamic loading protocol. Note that the quasi-static loading protocol (i) is typically used to examine the displacement-sensitive systems or components, for which the damage is related to the lateral drift. As the stone panels have relatively heavy mass, the inertial force induced by large acceleration would lead to additional force demand to undercut bolt connections. Therefore, the dynamic loading protocol (ii) was considered in the tests, to examine the possible adverse influence of the acceleration and corresponding inertial force. Furthermore, the SCWS in a real-world building is subjected to bi-directional loading in an earthquake event, and the out-of-plane loading would result in additional demand to the connection (e.g., the pull-out force of the undercut bolts). As such, the bi-directional dynamic loading protocol (iii) was included in the tests as well.

2.3.1 FEMA 461 quasi-static loading protocol

The loading protocol according to FEMA 461 is illustrated in FIGURE 5. The first loading amplitude of drift angle was 0.1%, with a lateral displacement of 3.2 mm. The loading rate was approximately 1 mm/s. The loading amplitude at each step was increased by 1.4 times. In FIGURE 5, Δ_m denotes the maximum targeted displacement amplitude of the loading history, which is the point at which the most severe damage was expected to occur.

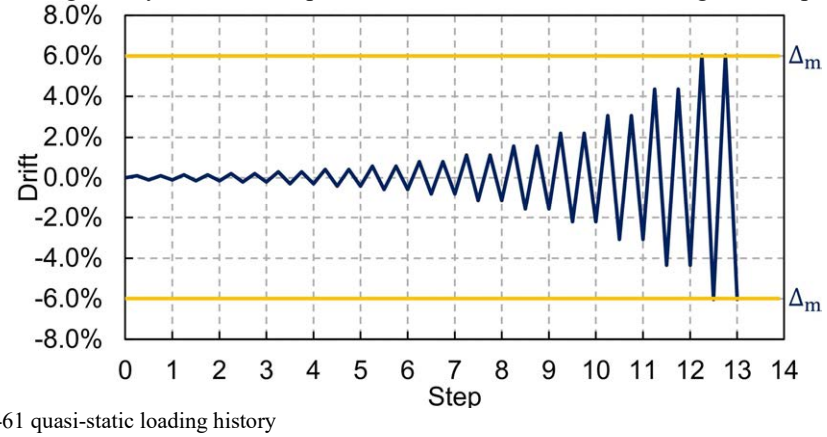

FIGURE 5 FEMA 461 quasi-static loading history

2.3.2 AAMA 501.6-01 dynamic loading protocol

AAMA 501.6-01 recommends a dynamic test method for determining the seismic drift capacity of curtain wall systems. The AAMA501.6-01 loading protocol, which is specific to a glass curtain wall system, was used in this study for the dynamic loading of the SCWS. As illustrated in FIGURE 6, the AAMA 501.6-01 loading protocol comprised concatenated 'ramp-up' and 'constant amplitude' intervals, where each interval consisted of four sinusoidal cycles. Furthermore, the in-plane racking displacement steps between constant amplitude intervals were 6 mm. The loads in this study consisted of two phases. The first phase was conducted at a frequency of 0.8 Hz with lateral displacements ranging from 0 to 72 mm, following which the second phase was performed at a frequency of 0.4 Hz with lateral displacements ranging from 72 to 160 mm.

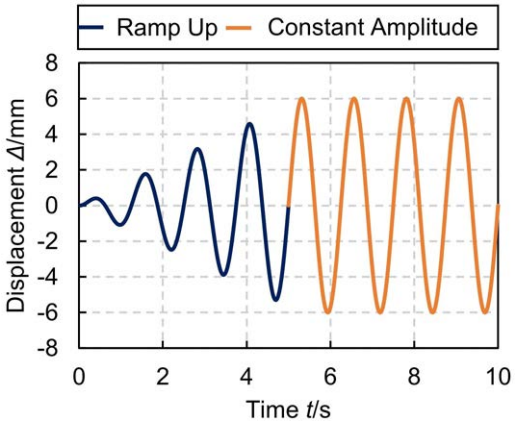

(a) First eight cycles

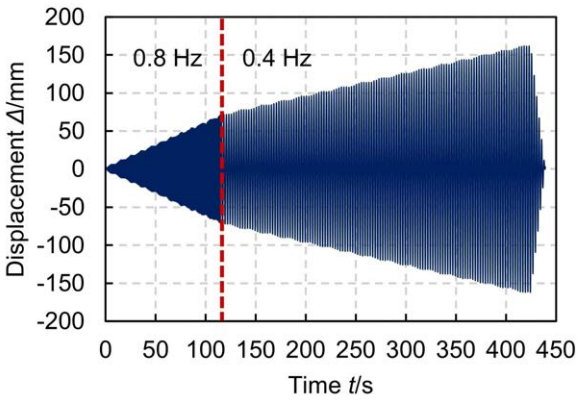

(b) Full time history

FIGURE 6 AAMA 501.6-01 dynamic loading history[23]

2.3.3 Bidirectional AAMA 501.6-01 loading protocol

There is no recommended bidirectional dynamic loading protocol specifically suitable for the SCWS. In this study, a bidirectional loading protocol based on the AAMA 501.6-01 standard proposed by Ji et al.[23] [22]was adopted. In this loading protocol, loads in both directions were sinusoid motions, with identical displacement amplitude and no phase lag in both in-plane and out-of-plane directions. The in-plane displacement response and out-of-plane displacement response reached their maximum simultaneously, ensuring that the stone curtain wall system experienced the most critical bidirectional loading conditions.

As identified from the white noise excitation data, the natural vibration frequency of the entire test system at the initial status was 1.6 Hz for the in-plane direction and 1.3 Hz for the out-of-plane direction. To ensure that the SCWS specimen reproduced the lateral drift history in the loading protocol, a specific shaking table input was generated by the inverse linear dynamic analysis, as detailed in Ji et al.[23]. Taking into consideration the oil supplement limitation of the shake table, the entire load protocol was divided into three segments, where the first two segments had a loading frequency of 0.8 Hz and the last segment had a loading frequency of 0.9 Hz.

3 EXPERIMENTAL RESULTS

3.1 Test 1: FEMA 461 quasi-static loading test

Specimen SCW1 was loaded using the FEMA 461 quasi-static loading protocol. In this test, the loading drift ratio θ gradually increased from 0.1% to 4.4%. At 0.4% drift loading, the gaskets between the aluminum alloy connector and L-shaped steel angle extruded (FIGURE 7a). At 2.8% drift loading, disengagement of the connectors from the L-shaped steel angle was observed (FIGURE 7b). At 3.1% drift, rotation of the connectors (FIGURE 7c) and obvious misalignment of the stone panels (FIGURE 7d) were observed, while an increased number of connectors were found to be disengaged from the steel angle. Due to the connections with surrounding silicone sealant, stone panels that no longer had the support of L-shaped steel angles did not fall out. At the first cycle of 4.4% drift loading, a column of stone panels on the south SCWS fully detached from the transoms, as depicted in FIGURE 7e. Upon the second cycle of 4.4% drift loading, the welds at the transom-to-mullion connection fractured, resulting in a complete failure of the supporting frames and consequent falling of the south SCWS (FIGURE 7f). Note that, no stone panels on the north SCWS fell out at 4.4% drift loading, although fracture of the silicone sealant was clearly observed (FIGURE 7g). In addition, no damage occurred at the surface of the stone panel and the undercut bolts during the test.

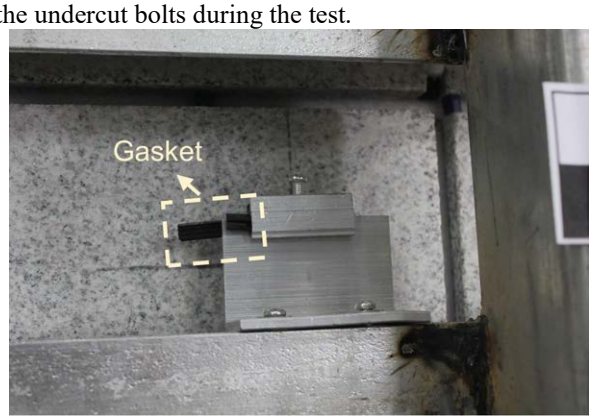

(a) Extrusion of gaskets

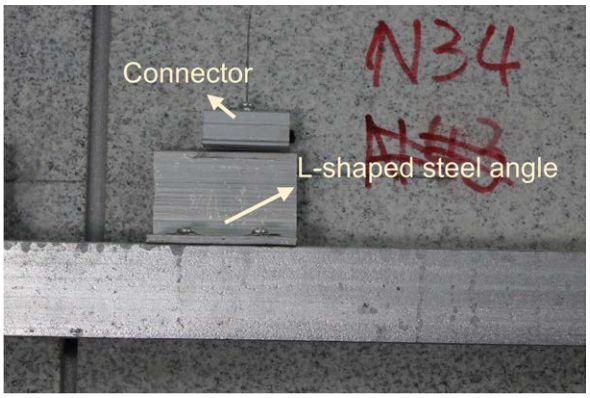

(b) Disengagement of connector

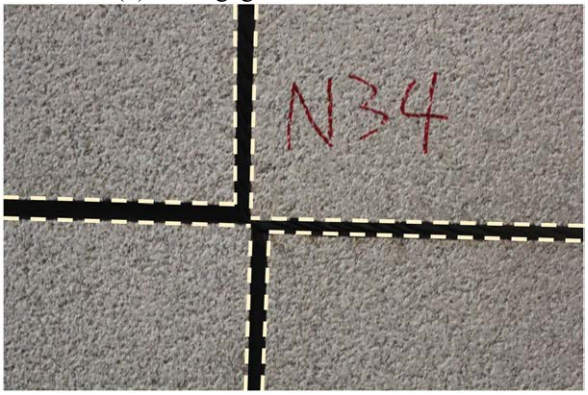

(c) Rotation of connector

(d) Misalignment of stone panels

(e) Detachment of a column of stone panels

(f) Falling of the south curtain wall

(g) Fracture of the silicone sealant of the north curtain wall

FIGURE 7 Photographs of the damaged specimen (FEMA 461 quasi-static loading test)

FIGURE 8 depicts the force-displacement hysteretic response of the specimen. Prior to 0.7% drift loading, the SCWS remained elastic. The specimen reached its peak strength capacity at 2.2% drift. When the drift increased, the lateral stiffness and strength gradually decreased due to the failure of connections.

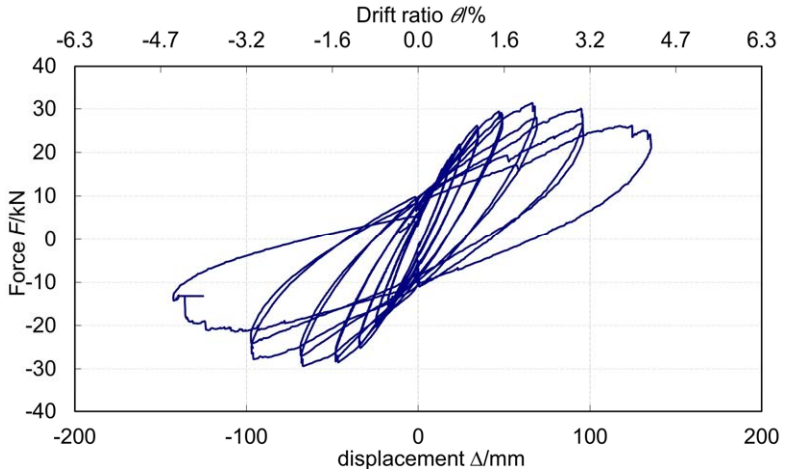

FIGURE 8 Hysteretic curve of SCW1 (FEMA 461 quasi-static loading test)

3.2 Test 2: AAMA 501.6-01 loading test

The damaged specimen that experienced FEMA 461 loading was repaired by re-welding the damaged transom-to-mullion connection, adjusting the position of the stone panels and filling the cracked silicone sealant. Because the south curtain wall completely fell and some stone panels were broken, only two columns of stone panels were recovered. Having completed the repair, the specimen was loaded following the AAMA 501.6-01 loading protocol. As illustrated in FIGURE 9, the applied lateral load was divided into two phases due to limitations in the oil supplement to the actuator. In the first phase, the loading frequency was 0.8 Hz, with the lateral drift amplitude gradually increasing from 0 to 72 mm (θ = 2.4%). In the second phase, the loading frequency was 0.4 Hz, with the lateral drift amplitude increasing from 72 mm to 160 mm (θ = 2.4% - 5.3%). At 0.8% drift loading, misalignment of the stone panels was observed. At 2.6% drift loading, disengagement of connectors was observed. Simultaneously, the transom at the fifth row of the north curtain wall fell off due to the fracture of transom-to-mullion welds, resulting in the "rolling shutter" style falling of this wall (FIGURE 10a). At 3.7% drift loading, the south stone panels fell down together with the transoms (FIGURE 10b). The damage process and failure mode of the specimen under the AAMA 501.6-01 loading test were almost identical to those observed in the FEMA 461 quasi-static loading test, indicating minimal influence of the loading rate.

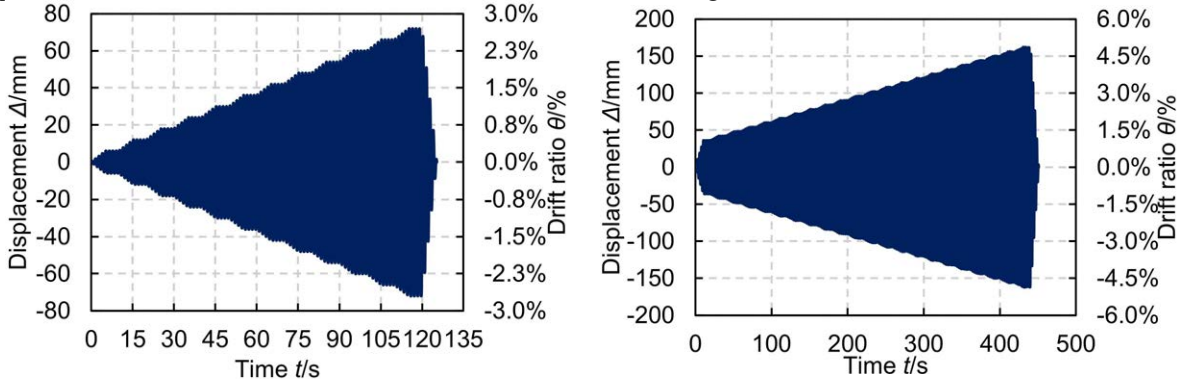

(a) Phase 1: 0.8 Hz (b) Phase 2: 0.4 Hz

FIGURE 9 Time history of AAMA 501.6-01 loading test

(a) North curtain wall (b) South curtain wall

FIGURE 10 Photographs of damaged specimen (AAMA 501.6-01 loading test)

The equation of motion that represents this dynamic test system is as follows:

$$m\ddot{x} + c\dot{x} + f(x) = F_{\text{actu.}} \tag{1}$$

where $F_{\text{actu.}}$ represents the dynamic lateral force exerted by the actuator, which was measured by a load cell installed at the end of the actuator; $m\ddot{x}$ denotes the inertial force and $c\dot{x}$ denotes the damping force; $f(x)$ represents the restoring force provided by the stone curtain wall system, which can be obtained by F_{actu} - $m\ddot{x}$ neglecting the damping force $c\dot{x}$. FIGURE 11 displays the lateral force-displacement hysteretic responses of the stone curtain wall system specimen in the AAMA 501.6-01 dynamic loading test. During the first phase of loading, the effective stiffness of the curtain wall started to degrade at 0.8% drift. At 1.3% drift loading, the strength capacity reached

its peak. At the same time, the effective stiffness experienced a further decrease due to disengagement of the connectors. During the second phase of loading, the stone curtain wall experienced a significant degradation in stiffness and strength capacity when the drift ratio exceeded 2.4%— this was attributable to the fracture of transom-to-million welds and falling out of stone panels.

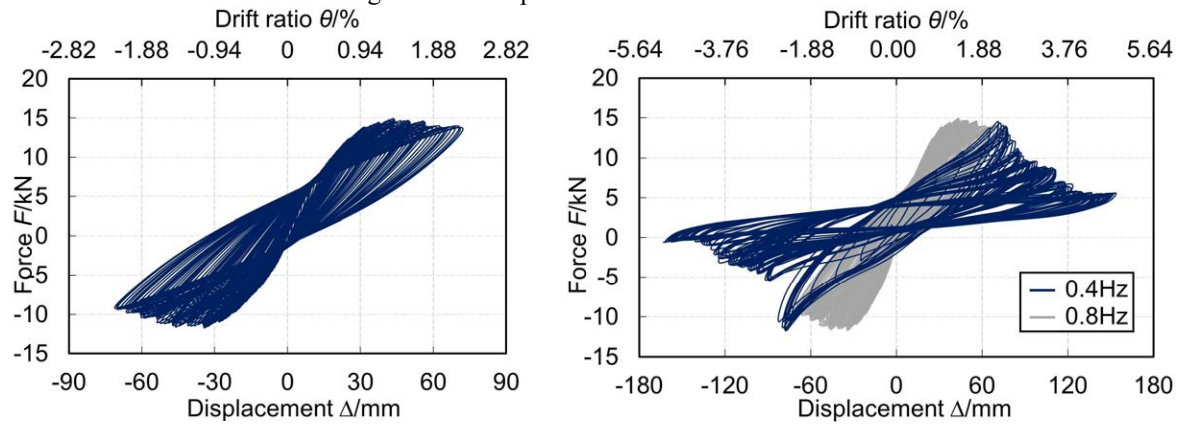

(a) Phase I of Test 2 (0.8 Hz) (b) Phase II of Test 2 (0.4 Hz)

FIGURE 11 Restoring force f(x) - displacement Δ hysteretic curve for Test 2

3.3 Test 3: Bidirectional AAMA 501.6-01 loading test

The bidirectional test system described in Section 2.2 Test set-upwas utilized for this test and included a total of three loading segments. The amplitude and frequency of each sinusoid motion segment are detailed in TABLE 2.

TABLE 2 Summary of each loading segment

Segment	Target displacement /mm	Frequency /Hz	Measured maximum response			
			In-plane		Out-of-plane	
			Drift ratio /%	Acceleration /g	Drift ratio /%	Acceleration /g
1#	0–30	0.8	1.07	0.41	0.86	0.18
2#	30–60	0.8	2.20	0.71	1.61	0.30
3#	60–90	0.9	5.43	1.63	5.65	1.41

No visible damage was observed in loading Segments 1# and 2#. However, during the loading of Segment 3#, resonance occurred as the natural frequency of the specimen gradually decreased to approach the excitation frequency. Consequently, the maximum in-plane and out-of-plane drift ratio reached 5.43% and 5.65%, respectively, and the peak in-plane and out-of-plane acceleration was 1.63 g and 1.41 g, respectively. At 3.3% drift loading, the lower connectors in the southern curtain wall detached from the L-shaped steel angle. At the end of the loading test, fracture of the silicone sealant and disengagement of the connectors were observed. Notably, although no stone panels fell out, significant damage resulted in instability of the curtain wall system. FIGURE 12 displays photographs of the damaged specimens after testing.

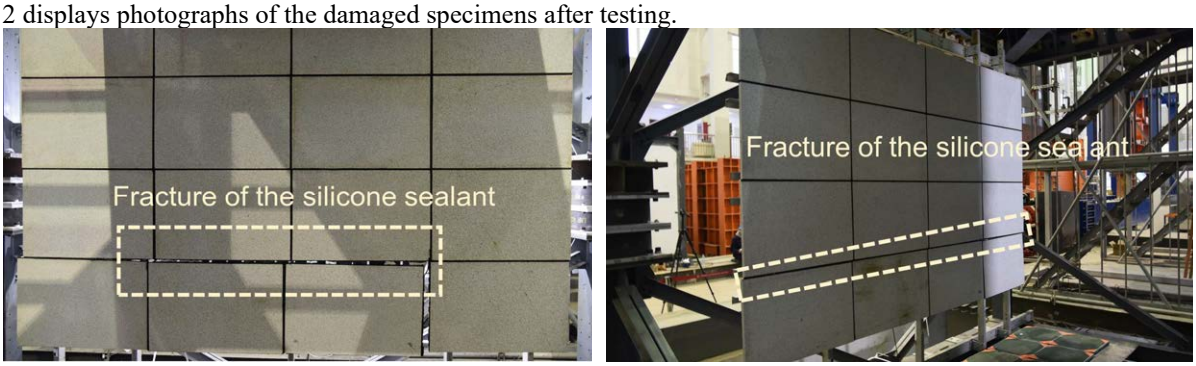

(a) South curtain wall (b) North curtain wall

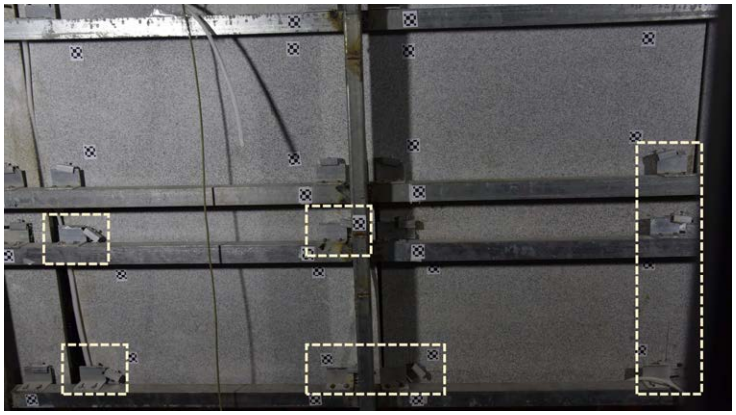

(c) Disengagement of connectors from L-shaped steel angles

FIGURE 12 Photographs of damaged specimen after the bidirectional AAMA 501.6-01 loading test

3.4 Summary of experimental tests

The SCWS exhibited an identical failure mode under in-plane quasi-static loading protocol, in-plane dynamic loading protocol and bidirectional dynamic loading protocol. The failure of the SCWS was mainly due to disengagement of the connector, followed by fracture of the silicone sealant and transom-to-mullion connection welds, and the eventual falling out of stone panels. The drift associated with disengagement of the connector during in-plane quasi-static loading and in-plane dynamic loading was 2.8% and 2.6%, respectively. The increased cycles of drift loading and in-plane acceleration in this test did not appear to expedite the disengagement of the connector from the L-shaped steel angle.

The falling out of stone panels in the north and south SCWS occurred at 2.6% and 3.7% drift for Test 2, respectively. Therefore, the average drift ratio associated with stone panels falling out during Test 2 was 3.2%, which was less than the falling out drift of 4.4% for Test 1. Because the falling out of stone panels in both tests was eventually caused by fracture of the transom-to-mullion connection, the lower drift at failure in Test 2 was attributed to the low-cycle fatigue effect of connection welds. Each loading interval consisted of two cycles for Test 1 and eight cycles for Test 2. As a result, increased cycles of loading led to earlier fracture at the transom-to-mullion welds and consequent falling of the SCWS in Test 2.

It is notable that the failure of the SCWS was primarily caused by disengagement of the connectors from the L-shaped steel angles. Connectors only experience in-plane displacement due to the constraints imposed by the steel angle when their vertical overlap depth is sufficient FIGURE 13 **错误!未找到引用源。**a. However, re-engagement with the L-shaped steel angle becomes problematic if the connectors experience out-of-plane disengagement due to insufficient vertical overlap depth FIGURE 13 **错误!未找到引用源。**b. Furthermore, if the edge distance between the connectors and the L-shaped steel angles is insufficient, the connectors may become detached from the L-shaped steel angle under a large drift ratio, and hence are unable to return to their original position due to obstruction of the leveling bolts. Therefore, it is necessary to propose design details for the minimum overlap depth and edge distance between the connector and the L-shaped steel angle. Specific design recommendations for the connectors are discussed in Section 4.

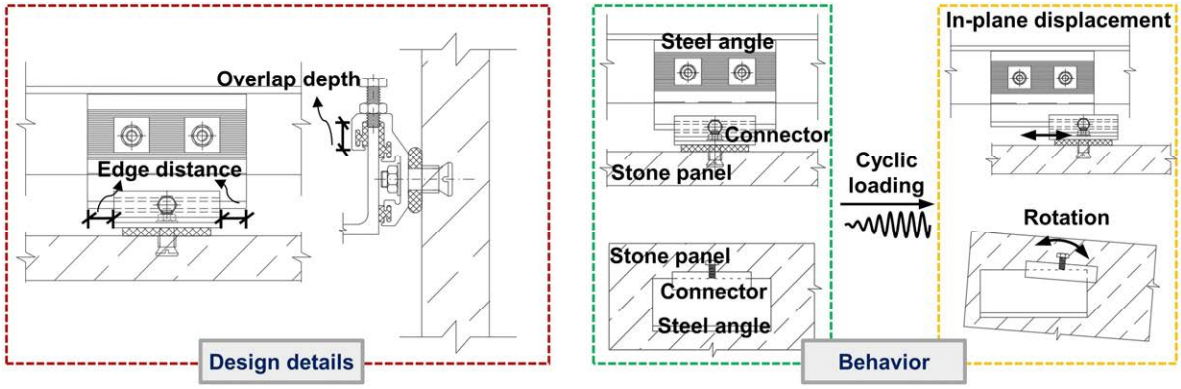

(a) Sufficient overlap depth and edge distance

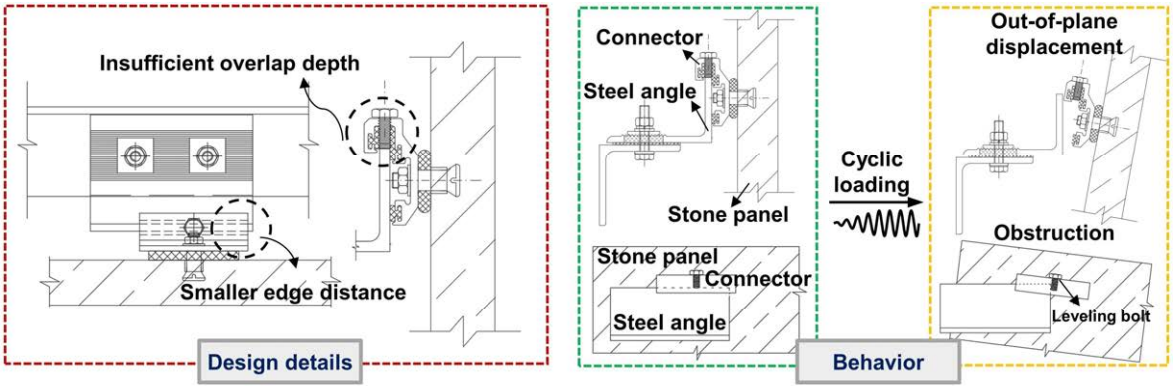

(b) Insufficient overlap depth and edge distance

FIGURE 13 Connector behavior

Notably, shear failure or anchorage failure of undercut bolts did not occur in the tests. According to Chinese standard DB11-T 512-2007 [11], U.S. code [10]ACI 318-19 [12], [11]and Canada code CSA A23.3 [13][12], the tensile and shear force demands of an undercut bolt are given by Equation (2) and Equation (3). The anchorage tensile and shear strength capacities of an undercut bolt are specified in Equation (4) and Equation (5).

$$N_{\mathrm{d}} = \frac{m\ddot{a}_{\mathrm{y}}}{n} \tag{2}$$

$$V_{\mathrm{d}} = \sqrt{\left(\frac{G}{n}\right)^2 + \left(\frac{m\ddot{a}_{\mathrm{x}}}{n}\right)^2} \tag{3}$$

$$N_{\mathrm{c}} = \min(N_{\mathrm{t}}, N_{\mathrm{max}}) = \min\left(f_{\mathrm{y}}A_{\mathrm{b}}, \beta_{\mathrm{zp}}f_{\mathrm{cu}}^{0.5}H_{\mathrm{ey}}^{1.5}\right) \tag{4}$$

$$V_{\mathrm{c}} = 0.58f_{\mathrm{y}}A_{\mathrm{b}} \tag{5}$$

where N_{d} and V_{d} denote the tensile force demand and shear force demand, respectively; N_{c} represents the tensile strength capacity of the undercut bolt; V_{c} denotes the shear strength capacity of the undercut bolt; N_{max} represents the design anchorage tensile strength capacity of the undercut bolt at the stone panel; m denotes the mass of the stone panel; $\ddot{a}_{\mathrm{x}}$ and $\ddot{a}_{\mathrm{y}}$ denotes the in-plane and out-of-plane acceleration of the curtain wall system in the test, respectively; G represents the weight of the stone panel; n denotes the number of undercut bolts for a stone panel; f_{y} represents the yield strength of the undercut bolt; A_{b} denotes the cross-sectional area of the undercut bolt; f_{cu} represents the compressive strength of the stone (unit in MPa); H_{ey} denotes the effective anchorage depth of the undercut bolt, which is equal to H - 1, where H represents the anchorage depth of the undercut bolt (unit in mm); and β_{zp} represents a factor which is taken as 12.5 if the effective anchorage depth of the undercut bolt H_{ey} is greater than 15 mm, and taken as 10.0 if the H_{ey} is less than 15 mm.

The calculations indicated that the maximum tension and shear force demands of the undercut bolts among all tests were 130.6 N and 177.3 N, respectively. Using the nominal yield strength of M6 bolt (f_{y} = 320 MPa) and the nominal compressive strength of Granite MU150 stone (f_{cu} = 150 MPa), the anchorage tensile strength capacity and strength capacity of the undercut bolts were calculated as 5248 N and 3873 N. As the tensile and shear force demand was significantly smaller than the corresponding strength capacity, damage to the undercut bolt connections would be unlikely to occur in the testing stone curtain wall system. This is the reason why the in-plane dynamic loading scenario and the bidirectional dynamic loading scenario did not result in the shear failure or anchorage failure of undercut bolts, although they led to increased force demand to the undercut bolt connection.

4 BEHAVIOR AND DESIGN IMPLICATIONS OF CONNECTORS IN SCWS

4.1 Connector behavior observed in tests

The connectors underwent in-plane horizontal and vertical displacements relative to the L-shaped steel angles. The relative displacement was identified from the test video using a computer vision technique[23] [24] in which a deep learning based dense optical flow method was used to track the displacement of the region of interest (ROI). The relative motion of each pixel between the initial frame and the current frame of the video was predicted using a pretrained deep learning model. The sub-pixel displacement of the ROI was then determined by averaging the pixel movements within the ROI. The physical displacement of the ROI was calculated through unit conversion using a reference object with known dimensions. As depicted in FIGURE 14, regions on the stone panels adjacent to the connectors (blue block) and regions on the transoms adjacent to the L-shaped steel angle (red block) were chosen as the ROIs, and the identified displacements of those ROIs were used to represent the displacements of

the connectors and angle steel, respectively. By subtracting the connector displacement from the angle steel displacement, the relative displacement between the connector and the L-shaped steel angle was obtained.

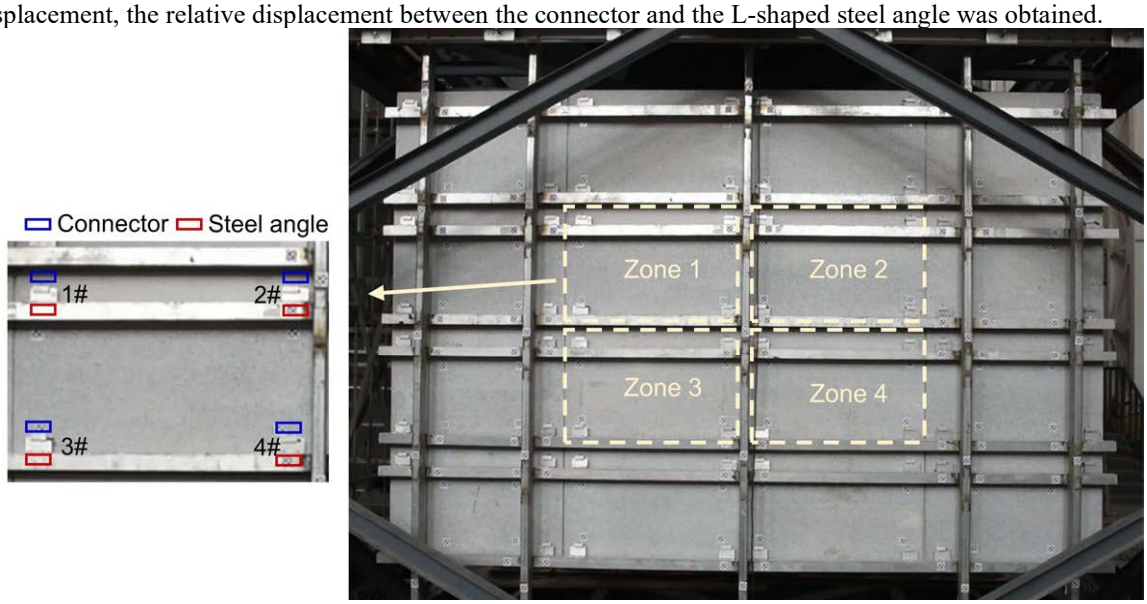

FIGURE 14 Photographs of the stone curtain wall in Segment 3# loading videos

FIGURE 15 illustrates the horizontal and vertical relative displacement of the typical connector in four zones (see FIGURE 14) of the south SCWS in Segment 3# of Test 3. This indicates that the relative displacement of the connectors increased in line with an increase in the drift ratio. The relative horizontal displacement was greater than the vertical displacement. Moreover, horizontal residual displacements after bidirectional loading ranged from about 3 mm to 15 mm. There was no obvious vertical residual displacement.

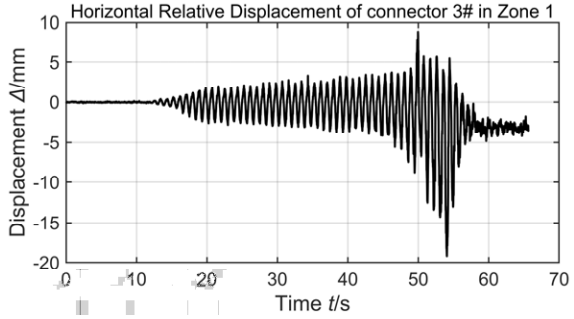

(a) X-direction (Zone 1)

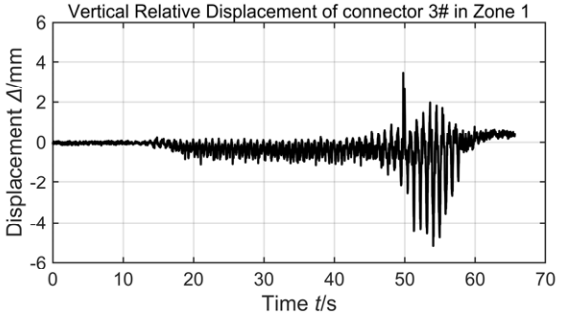

(b) Y-direction (Zone 1)

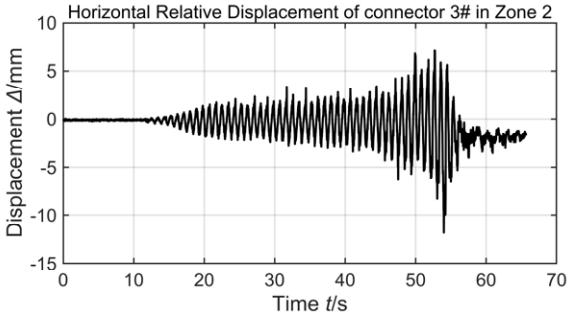

(c) X-direction (Zone 2)

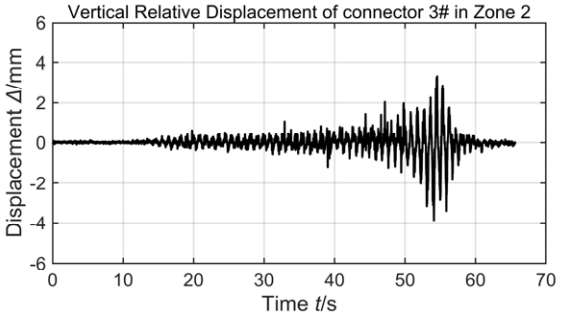

(d) Y-direction (Zone 2)

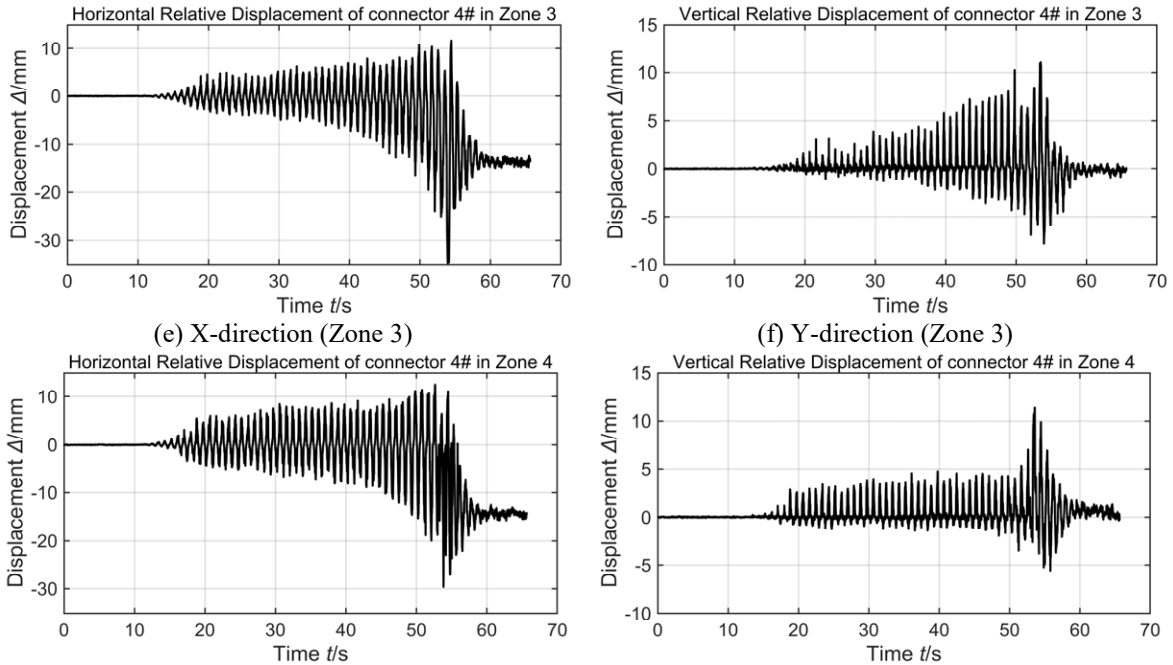

(e) X-direction (Zone 3) (f) Y-direction (Zone 3)

(g) X-direction (Zone 4) (h) Y-direction (Zone 4)

FIGURE 15 Displacement of connectors

4.2 Calculation of connector displacement demand

Calculation models were developed in order to describe the relationship between the horizontal and vertical relative displacements of the connectors and the inter-story drift ratio. The relative displacements of the connectors were extracted before the drift ratio reached 3.0%, at which point the specimens remained stable without significant damage.

4.2.1 Calculation of connector horizontal relative displacement

FIGURE 16 illustrates the relationship between the horizontal relative displacements of the upper and lower connectors. As illustrated in FIGURE 16a (referred to as Case 1), if one assumes that the upper connectors are fixed to the transom without any sliding, the horizontal relative displacement of the lower connectors is equal to θh where θ denotes the inter-story drift ratio and h represents the distance of two adjacent transoms hanging one panel. Conversely, if one assumes that the lower connectors are fixed to the transom, the horizontal relative displacement of the upper connectors is $-\theta h$, as shown in FIGURE 16b (referred to as Case 2). In reality, both the upper and lower connectors developed sliding, as displayed in FIGURE 16c, where the magnitude of sliding displacement needed to satisfy Equation (6), while the maximum sliding displacement between the upper and lower connectors was calculated using Equation (7).

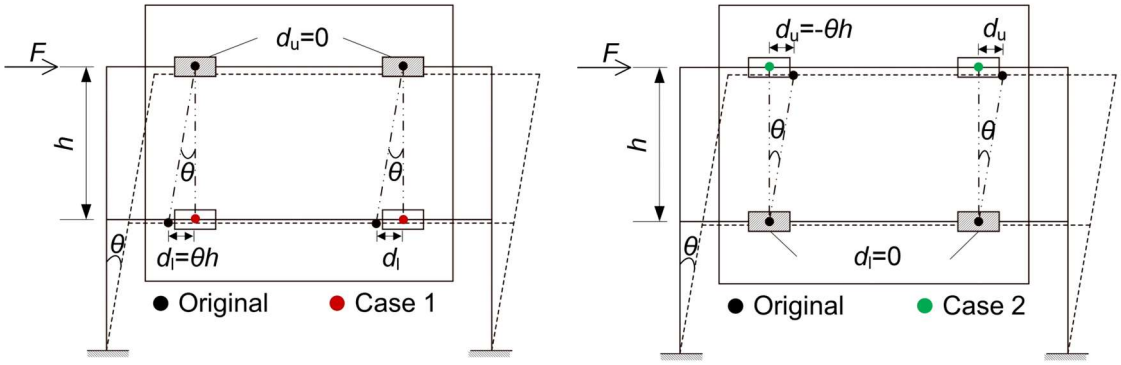

(a) Case 1 (b) Case 2

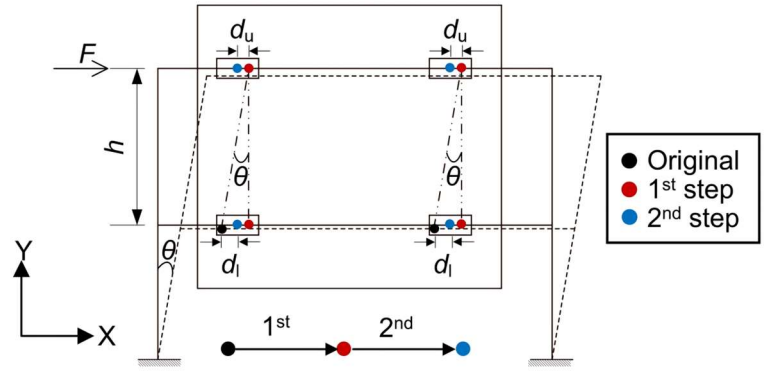

(c) Realistic situation

FIGURE 16 Horizontal relative displacement of the connector

$$|d_u| + |d_l| = \theta h \tag{6}$$

$$d_h = \alpha_{max}\theta h = \max(\alpha, 1-\alpha)\theta h \tag{7}$$

where d_u and d_l denote the relative horizontal displacement of the upper connector and lower connector, respectively; α is a factor that represents the ratio of the upper connector sliding displacement; and α_{max} denotes the larger factor between the ratio of the upper and lower connector sliding displacement.

In addition, the stone panel exhibited a rigid rotation, which in turn reduced the horizontal displacement demand on the connectors. Therefore, Equation (7) can be further updated by considering the influence of panel rigid rotation to give:

$$d_h = \alpha_{max}(\theta - \theta_r)h \tag{8}$$

where θ_r denotes the rigid rotation of the stone panel, which can be calculated from **错误!未找到引用源。** to **错误!未找到引用源。**.

$$\theta_{r_u} = \frac{\Delta_{u_left} - \Delta_{u_right}}{l} \tag{9}$$

$$\theta_{r_l} = \frac{\Delta_{l_left} - \Delta_{l_right}}{l} \tag{10}$$

$$\theta_r = \frac{\theta_{r_u} + \theta_{r_l}}{2} \tag{11}$$

where Δ_{u_left} and Δ_{u_right} represent the vertical displacement of the upper connector 1# and 2#, while Δ_{l_left} and Δ_{l_right} denote the vertical displacement of the lower connector 3# and 4# (see FIGURE 14), and l represents the distance between the left and right connectors of a single stone panel.

As indicated in FIGURE 17a, the rigid rotation of stone panel θ_r exhibited an approximately linear increase in line with an increase in the inter-story drift θ. Therefore, it is assumed that $\theta_r = \gamma\theta$. The γ value can be obtained from test data, which follows a normal distribution, as depicted in FIGURE 17b. The mean value and standard deviation of γ was estimated as 0.30 and 0.002, respectively, using the maximum likelihood method. The probability distributions of γ were subjected to the Jarque-Bera test [25], [24]using a significance level of 0.05. The p-value for γ was 0.068, indicating that the goodness-of-fit test was satisfactory. The mean of the normal distribution of γ was selected as the representative value (γ = 0.30). Therefore, the formula for calculating the horizontal displacement of connectors d_h is given by Equation (12).

$$d_h = \alpha_{max}(1-\gamma)\theta h = 0.7\alpha_{max}\theta h \tag{12}$$

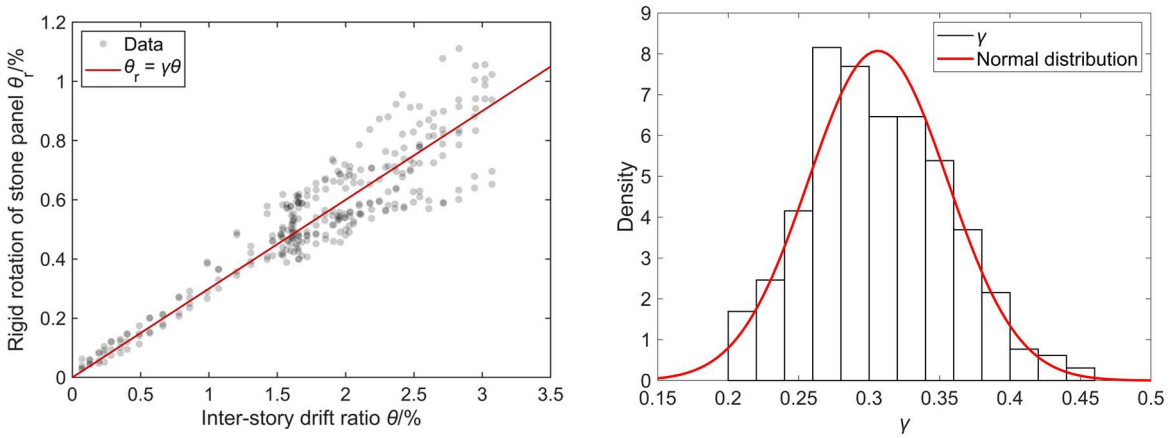

(a) Relationship between θ_r and θ (b) Distribution type

FIGURE 17 Data set of γ

Similarly, as depicted in FIGURE 18, the sample data for the coefficients α_{max} were determined from the data set of the larger relative horizontal displacement between the upper and lower connectors, which was calculated using Equation (12). The mean and standard error of α_{max} were 0.64 and 0.08, respectively. The upper 95% confidence interval for α_{max} was 0.80, calculated using Equation (13). Hence, the formula for calculating horizontal relative displacement was determined using Equation (14), and the relative horizontal displacement under a 95% confidence level was determined using Equation (15).

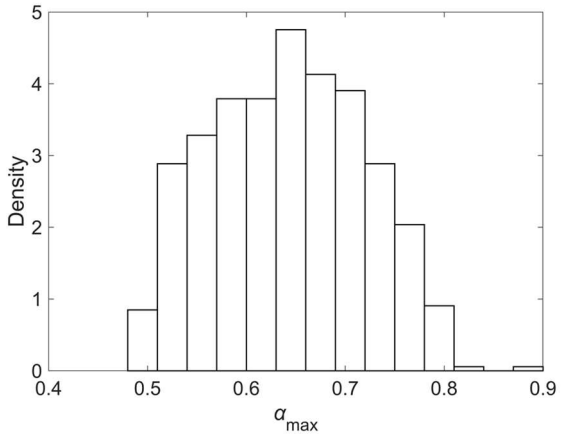

FIGURE 18 Data set of α_{max}

$$\alpha_{max}^{95\%} = \mu + 1.96\sigma \tag{13}$$

$$d_h = 0.7\alpha_{max}\theta h = 0.64 \times 0.7\theta h = 0.45\theta h \tag{14}$$

$$d_{h95\%} = 0.7\alpha_{max}^{95\%}\theta h = 0.7 \times 0.80\theta h = 0.56\theta h \tag{15}$$

where μ and σ denote the mean and standard error of α_{max}, and $\alpha_{max}^{95\%}$ represents the upper 95% confidence interval of α_{max}.

In this test, the distance between the upper and lower connectors of a single stone panel was 450 mm; thus, h = 450 mm. FIGURE 19 compares the relationship between the proposed model in this paper and the experimental data, revealing a good fit with the experimental results.

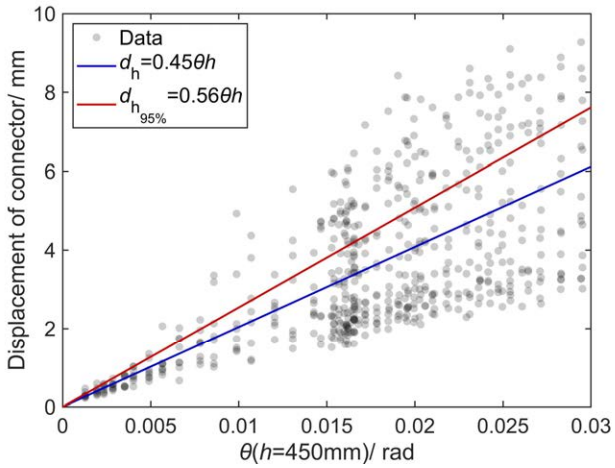

FIGURE 19 Horizontal relative displacement model

A notable point of concern was that the loading cycle numbers may have influenced the sliding displacement magnitude of the connectors. Therefore, the sliding displacement of data for the shaking table tests was analyzed using Equation (16) in order to investigate the possible effect of loading cycles. It is important to note that in the shaking table tests, each loading level included four cycles of constant amplitude loading. The horizontal relative displacements for constant amplitude loading at 1.6%, 2.0% and 2.4% drift were considered.

$$\beta_{\mathrm{m}} = \frac{1}{k-1}\sum_{i=1}^{3}\frac{d_{i+1}}{d_i} \tag{16}$$

where β_{m} represents the average ratio of the horizontal peak displacements of the connectors between the adjacent two cycles in the constant amplitude loading; m represents the connector number, with a total of 16 connectors; k denotes the number of cycles of constant amplitude loading which in this test was k = 4; and d_i represents the horizontal peak displacements of the connectors during the i-th cycle in each constant amplitude loading. As illustrated in FIGURE 20, the values of β_{m} were close to 1.0, indicating that the number of loading cycles had a negligible impact on the horizontal peak relative displacement of the connectors.

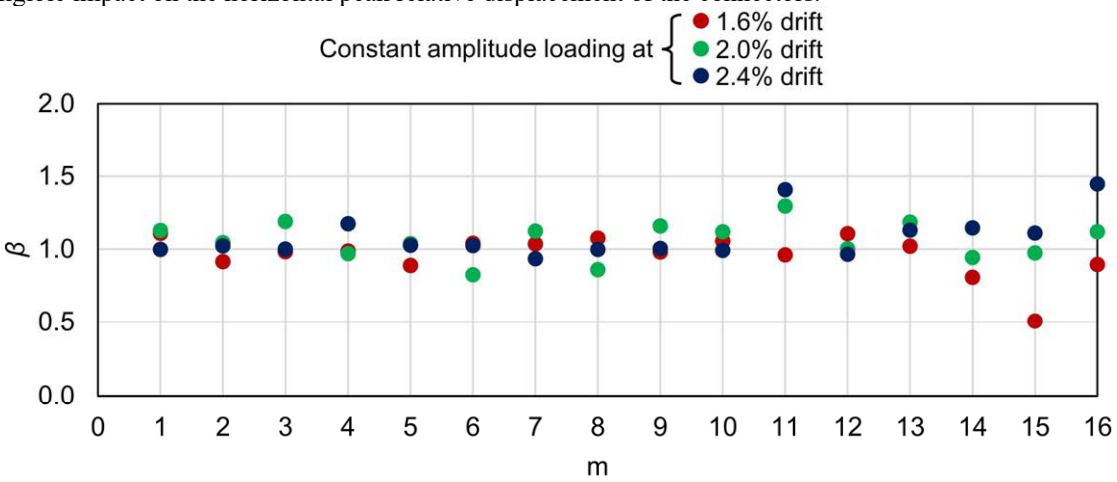

FIGURE 20 β_{m} under each constant amplitude loading step

4.2.2 Calculation of connector vertical relative displacement

The vertical relative displacement of the connector was principally caused by the rigid body rotation of the stone panel itself (see FIGURE 21). Assuming the stone panel rotated around the right (or left) connector (i.e., d_{v} = 0 at this rotation center connector), the vertical relative displacement of the left (or right) connector was calculated using Equation (17). Note that the test data indicated that the left and right connectors had opposite vertical displacements, and thus the aforementioned assumption would lead to somewhat overestimate to the vertical displacements.

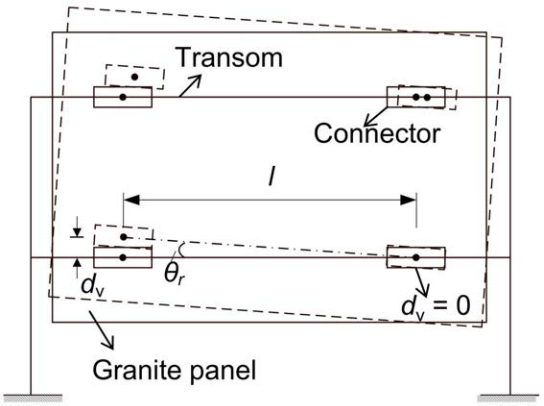

FIGURE 21 Vertical relative displacement of the connector

$$d_v = \theta_r l \tag{17}$$

where l denotes the distance between the left and right connectors of a single stone panel. Based on $\theta_r = 0.30\theta$, the vertical relative displacement was calculated using Equation (18).

$$d_v = 0.30\theta l \tag{18}$$

FIGURE 22 illustrates the relationship between the proposed model in this paper and the experimental data, indicating that the model enveloped the experimental data points and offered a conservative estimation. In this test, the value of l was equal to 765 mm.

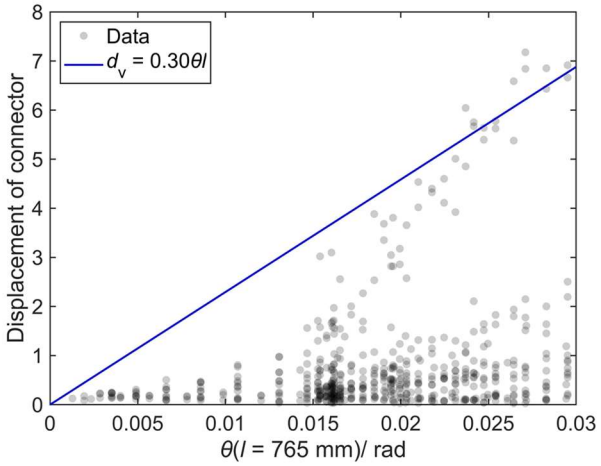

FIGURE 22 Vertical relative displacement model

4.3 Design recommendation for connectors

To prevent stone panels from falling out, connectors should not be detached from the steel angle under the maximum considered earthquake (MCE). According to the ASCE 7-22 [26] and 2020 LATBSDC Alternative Analysis and Design Procedure [27], the inter-story drift ratios of building structures under MCE ground motions should be no greater than 3.0%. For a drift equal to 3.0%, the maximum horizontal and vertical displacements of the connectors were $0.017h$ and $0.009l$, as calculated using Equation (15) and Equation (18). Consequently, to ensure that the connectors do not become detached from the steel angle, it is suggested that the distance from the edge of the connector to the nearest edge of the L-shaped steel angle, d_h, should be greater than $0.017h$, and that the vertical overlap depth (d_v) should be greater than $0.009l$, as shown in FIGURE 23.

For instance, in the test for this study, the values of h and l were equal to 450 mm and 765 mm, respectively. Under 3.0% drift loading, the maximum horizontal and vertical displacements of the connectors were calculated as 7.7 mm and 7.0 mm, respectively. To prevent the stone panel from falling out, the horizontal distance d_h and vertical overlap depth d_v should be greater than 7.7 mm and 7.0 mm, respectively.

Except for the stone curtain walls, some other curtain walls (e.g., porcelain curtain walls and micro-crystal glass curtain walls) also often use the undercut bolts and connectors for connecting the panels to the supporting frame. While the panel materials are different from stones, they would suffer from the failure induced by the

disengagement of the connectors from the L-shaped steel angles. Therefore, the design recommendation obtained from this study can be applied to those types of curtain walls as well.

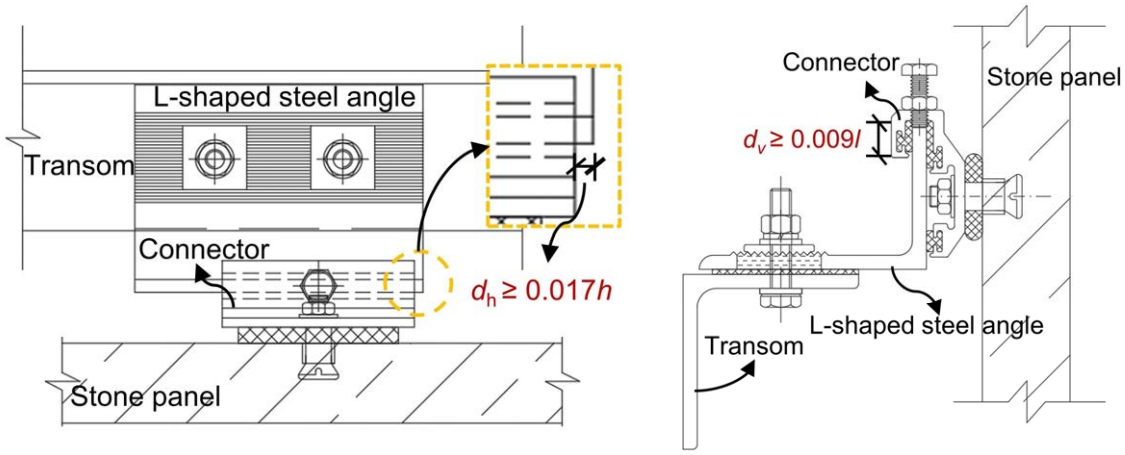

(a) Horizontal overlap distance (b) Vertical overlap distance

FIGURE 23 Requirements for connector design

5 CONCLUSIONS

In this study, quasi-static and dynamic tests were conducted on a full-scale stone curtain wall system with undercut bolt anchorage (SCWS-UBA) using two sets of loading systems. A method for calculating connector horizontal and vertical displacement was developed in order to provide practical design recommendations. The main conclusions from the study are as follows:

(1) The SCWS specimens exhibited an identical failure mode under in-plane quasi-static loading, in-plane dynamic loading, and coupled in-plane and out-of-plane dynamic loading. The failure of SCWS was primarily caused by disengagement of the connectors from the L-shaped steel angles, followed by fracture of the silicone sealant and transom-to-mullion connection welds and, finally, the falling out of stone panels.

(2) The SCWS-UBA specimens exhibited a large drift capacity. In all tests, the specimens had an ultimate falling out drift exceeding 3.0%. Thus, the drift capacity of the SCWS-UBA specimens is greater than the inter-story drift ratio requirement for building structures under MCE ground motions.

(3) Damage to the stone curtain walls was related to drift ratio rather than accelerations. For in-plane loading, disengagement of the connector occurred at a nearly identical drift ratio for both quasi-static loading (2.8%) and dynamic loading (2.6%).

(4) The failure of the SCWS-UBA was mainly due to insufficient horizontal edge distance and vertical overlap depth between the connector and the L-shaped steel angle. According to the formula of connector displacement proposed in this paper, the distance from the edge of the connector to the nearest edge of the L-shaped steel angle (d_h) should be greater than $0.017h$, and the vertical overlap depth (d_v) should be greater than $0.009l$ to prevent the stone panels from falling out, where h denotes the distance of two adjacent transoms hanging one panel and l represents the distance between the left and right connectors of a single stone panel.

ACKNOWLEDGEMENTS

The work presented in this paper was supported by the funds from the National Natural Science Foundation of China (Grant No. 52425808) and the National Key R&D Program of China (Grant No. 2018YFC1504401). The authors are sincerely grateful for the financial support.

REFERENCES

[1] Goodno B, Craig J, Zeevaert-Wolff A. The Mexico earthquake of September 19, 1985- behavior of heavy cladding components. *Earthquake spectra*. 1989; 5(1):195-222.

[2] Taly N. The whittier narrows, California earthquake of October 1, 1987 - performance of building at California State University, Los Angeles. *Earthquake spectra*. 1988; 4(2):277-317.

[3] EERI. *Northridge Earthquake preliminary reconnaissance report*. Earthquake Engineering Research Institute; 1995.

[4] Baird A, Palermo A, Pampanin S. Façade damage assessment if multi-storey buildings in the 2011 Christchurch earthquake. *Bulletin of the New Zealand Society for earthquake engineering*. 2011; 44(4):368-

76.
[5] Henry R, Ingham J. Behaviour of tilt-up precast concrete buildings during the 2010/2011 Christchurch earthquakes. *Structural Concrete*. 2011; 12(4): 234-240.
[6] Liberatore L, Sorrentino L, Liberatore D, et al. Failure of industrial structures induced by the Emilia (Italy) 2012 earthquakes. *Engineering Failure Analysis*. 2013; 34: 629-647.
[7] Toniolo G, Colombo A. Precast concrete structures: the lessons learned from the L'Aquila earthquake. *Structural Concrete*. 2012; 13(2): 73-83.
[8] Farmer MC, Lyons SP. Stone cladding failure: the cause and consequences. *Forensic Engineering*. 2000; 472-81.
[9] Ministry of Construction of the People's Republic of China. *Technical code for metal and stone curtain walls engineering (JGJ 133-2001)*. China Architecture & Building Press; 2001.
[10] American Society for Testing and Materials. *Standard specification for granite dimension stone* (*C615/C615M-11)*. ASTM International; 2011.
[11] Beijing Municipal Bureau of Construction. *Technical specification for application of stone in decoration (DB11-T 512-2007)*. China Architecture & Building Press; 2007.
[12] ACI. Building Code *Requirements for structural concrete (ACI 318-19) and commentary (ACI 318R-19)*, American Concrete Institute; 2019.
[13] CSA. *Design of concrete structures (CAN/CSA A23.3-94)*. Canadian Standards Association; 2024.
[14] Gao Z. Research on Connection Performance of Kerf Anchorage and Undercut Anchorage Stone Cladding Panels. Beijing University of Civil Engineering and Architecture; 2020. [in Chinese]
[15] Zhang, Q. Post-cut back-bolted point connection granite curtain wall. *Stone Material*. 2003(1):9-14. [in Chinese]
[16] Huang B, Lu W, Mosalam KM. Shaking table testing of granite cladding with undercut bolt anchorage. *Engineering Structures*. 2018; 171:488-499.
[17] Fan Y, Lu W, Yuan M, et al. A modified full-scale experimental method on the seismic performance of complex façade system. *Journal of Earthquake Engineering*. 2023;27(15):1-21.
[18] Lu W, Huang B, Cao W. Study on the shaking table test of micro crystal glass curtain wall. *Building Structure*. 2010;40(1):59-61. [in Chinese]
[19] Wang M, Hao R. Seismic test research on back-bolted stone curtain wall connections. *Building Structure*. 2001;31(4):70. [in Chinese]
[20] Xu Z, Zhou F, Jiang Q, et al. Seismic test research on the connection performance of dry-hung granite curtain walls using shake table simulation. *World Information on Earthquake Engineering*. 1999;15(4):41-51. [in Chinese]
[21] Zhou G, Xu Y, Wang M. Seismic test research on large-scale stone curtain walls. *Building Structure*. 2003;33(8):62-63. [in Chinese]
[22] Xin Z. The Analysis of the anti seismic test and the construction strength of super standard stone materials in the curtain wall engineering. Harbin Engineering University; 2004. [in Chinese]
[23] Ji X, Zhuang Y, Lim W, et al. Seismic behavior of a fully tempered insulating glass curtain wall system under various loading protocols. *Earthquake Engineering & Structural Dynamics*. 2024;53(1):68-88.
[24] Gao X, Ji X, Zhang Y, et al. Structural displacement estimation by a hybrid computer vision approach. *Mechanical Systems and Signal Processing*. 2023; 204:110754.
[25] Jarque CM, Bera AK. A test for normality of observations and regression residuals. *International Statistical Review/Revue Internationale de Statistique*. 1987;55(2):163-172.
[26] ASCE. *Minimum design loads for buildings and other structures (ASCE 7-22)*. American Society of Civil Engineers; 2022.
[27] LATBSDC. *An alternative procedure for seismic analysis and design of tall buildings located in the Los Angeles region*. Los Angeles Tall Buildings Structural Design Council; 2020.